Late Holocene initiation of a deep rock slope failure in an alpine valley revealed by 10Be surface exposure dating (Chamonix, France)

L. Courtial-Manent, Jean-louis Mugnier, S. Zerathe, J. Carcaillet, R. Vassallo, L. Ravanel, L. Tavernier, Jean-François Buoncristiani

Late Holocene initiation of a deep rock slope failure in an Alpine valley revealed by ^{10}Be surface exposure dating (Chamonix, France)

L. Courtial-Manent[a,*], J-L. Mugnier[a], S. Zerathe[a], J. Carcaillet[a], R. Vassallo[a], L. Ravanel[b], L. Tavernier[b], J-F. Buoncristiani[c]

[a]*Institut des Sciences de la Terre (ISTerre), Université Grenoble Alpes, Université Savoie Mont Blanc, CNRS, IRD, IFSTAR, 38000, Grenoble, France*

[b]*EDYTEM, USMB, CNRS, France*

[c]*Université de Bourgogne, UMR 6282 - Biogéosciences, Dijon, France*

* Corresponding author.

E-mail address : lea.courtial-manent@univ-grenoble-alpes.fr (L. Courtial-Manent).

Abstract:

We studied a newly identified, multiple-kilometer-long rock slope failure in the Aiguilles Rouges massif (Chamonix valley, France). Owing to a high-resolution light detection and ranging (LiDAR) digital elevation model (DEM) and field work, we mapped morphostructures, including scarps, open fractures, and counterscarps. In some places, vertical offsets can reach tens of meters and crevasses can be meters wide. The evidence of gravitational activity (boulder displacements from analyses of archival satellite images) and the sharpness of the scarp outcrops together suggest very recent movements. These observations agree with ground displacement rates of a few millimeters per year estimated by interferometric synthetic aperture radar (InSAR) time series between 2014 and 2018. We sampled two vertical profiles along the top scarps to define the chronology of the slope failure using beryllium-10 (^{10}Be) surface exposure dating. Glacially polished surfaces cut by these gravitational scarps were also sampled to determine glacial retreat timing as well as to constrain the pre-exposure ^{10}Be inheritance. In total, 11 samples were studied.

Our results highlight a significant time lag (approximately 15 ka) between the first evidence of nonglacial activity and the initiation of the slope failure that happened 1.3–2.5 ka ago, depending on

the inheritance schemes. This suggests that the delayed opening of the crevasse is only one stage of a process that began when the valley was deepened and the glacial debuttressing is not the unique driving factor. This process of progressive failure of an excessively steep slope may continue, and the evolution of this slope failure may constitute a hazard for the upper part of the Chamonix valley.

Keywords: Alpine glacial valley; Rock slope failure; Cosmogenic radionuclide dating; Natural hazard; Chamonix valley

1. Introduction

Shapes of alpine valleys have been deeply influenced by glacial cycles involving glacier retreats and advances over the Quaternary period (Harbor et al., 1988; Herman et al., 2011). These processes have formed U-shaped valleys with steepening slopes that are rejuvenated by gravitational processes (Le Roux et al., 2009; Crosta et al., 2013; Riva et al., 2018). Glacial debuttressing and mechanical stress release have often been mentioned as causes that favor slope instabilities that can lead to large scale landslides or rock slope failures (Holm et al., 2004; Bigot-Cormier et al., 2005; Cossart et al., 2008; Ballantyne et al., 2014). Predisposing factors, such as lithology, rock mass characteristics, or geologic structures, play an important role in rock slope initiation and mountain slope evolution. There are many potential triggering factors for gravitational structures in mountainous regions, sometimes working together, such as exceptional rainfall episodes (Guzzetti et al., 2004; Pothérat and Effendiantz, 2009), seismic activity (Chen et al., 2005; Jibson et al., 2006), changes in groundwater regime (Pisani et al., 2010), or permafrost degradation (Ravanel and Deline, 2011). All these factors control the spatial and temporal evolution of the instabilities, the landscape morphologies (Crosta et al., 2013), and the risks these instabilities represent for human communities and infrastructures.

Rock slope failures (RSFs) such as rockslides, rock avalanches, or rockfalls, are common hazards in mountainous areas. Due to climate changes and thawing permafrost, the frequency and severity increase at high altitude and catastrophic events can occur (e.g. Ravanel and Deline, 2011).

Conversely, deep-seated gravitational slope deformations (DSGSD) or slow-moving rockslides generally do not seem to directly threaten humans. They evolve at slow displacement rates (several mm yr^{-1}) over long periods and are characterized by specific geomorphological features such as counterscarps, double ridges, trenches, and tension cracks (El Bedoui et al., 2009; Le Roux et al., 2009). DSGSDs may occur with a time lag relative to glacier disappearance (Hormes et al., 2008; Ivy-Ochs et al., 2009; Prager et al., 2009b), supporting the hypothesis that even when the glaciers retreat they undergo progressive failure in subcritical stress conditions (Eberhardt et al., 2004; Brideau et al., 2009; Riva et al., 2018). Although they can appear stable or metastable, they can be reactivated and record sudden accelerations (see a review in Pánek and Klimeš, 2016). Understanding the long-term evolution and identifying the triggers of such structures are thus keys to estimating potential hazards in the near future.

Geochronological investigations allow the understanding of the temporal evolution of large RSFs (e.g. Pánek, 2015; Pánek and Klimeš, 2016). In the last decade, cosmic ray exposure (CRE) dating method, such as with *in-situ* produced beryllium-10 (^{10}Be), has been widely applied either to boulders in ladslide debris deposits (e.g. Zeng et al., 2020) or along headscarp walls (e.g. Böhme et al., 2019). For instance, these applications revealed successive failure phases of RSFs on single site but with time lag between each event reaching several thousand years (e.g. Delgado et al., 2020), synchronicity of slope failures with past climate changes (e.g. Sepulveda et al., 2022), long-term progressive failure leading to landslide slipe rate increase (e.g. Schwartz et al., 2017), among others.

In this study, we investigated a large RSF recently identified in the Aiguilles Rouges massif (Chamonix valley, western European Alps, France). We used the ^{10}Be dating method to establish its long-term evolution. We also performed field mapping supported by aerial photograph analyses and the interpretation of the high-resolution light detection and ranging (LiDAR)-derived digital elevation model (DEM) to determine the geomorphology of the area and the relationship with RSF landforms. This paper has the following four aims: (i) to constrain the timing of the initiation of the RSF, (ii) to

explore the link with local glacier extension, (iii) to identify the driving and triggering factors of the RSF, and (iv) to evaluate the potential threat it represents for the downslope population.

2. Settings

2.1 Geographic context

The Aiguilles Rouges massif (ARM) is located on the northwestern side of the Chamonix valley (western European Alps, France), west of the Mont Blanc massif (4808 m above sea level, a.s.l.) and is part of the alpine external crystalline massifs (Fig. 1). The ARM stretches over 15 km from northeast to southwest and goes from 1000 m a.s.l. near Chamonix to 2965 m a.s.l. at the Aiguille du Belvédère. It includes the 3279-ha Aiguilles Rouges Nature Reserve created in 1974. The Chamonix valley is highly populated and plays host to numerous touristic and economic activities including an important railway line and an international road linking France to Italy and Switzerland.

Our study site, called the Argentière crevasse (Fig. 1), is located in the Chéserys area, upslope of the Argentière village.

The massif is divided into three parts. The upper part of the Reserve is characterized by vertical walls and numerous remnant glaciers and alpine lakes. Then, the rhododendron moor marks the transition between the forest and alpine meadows. A dense spruce forest covers the steep slopes of the lower part of the Reserve. In terms of geomorphology, the landscapes of the upper slopes have mainly been shaped by glacial erosion and paraglacial processes, whereas screes and rockfall deposits from periglacial processes are major components of the lower slopes. Fallen rocks can sometimes reach more than 50 m across. One of these gravitational structures has been known since the 19th century as the iconic Aiguillette d'Argentière (1893 m a.s.l.), a rock slice of approximately 25 m high separated from the rockwall (Fig. 2)

On the landscape, trimlines (Fig. 1) indicate that the area was covered by ice during the Last Glacial Maximum (approximately 21 ka ago; Clark et al., 2009) at approximately 2600 m a.s.l. (Coutterand

and Buoncristiani, 2006). Glacier thinning could have occurred very quickly after 16.6 ± 0.6 ka ago (Lehmann et al., 2020). Regional synthesis, mainly based on relative geomorphological analysis and relative chronology, suggest that the Col des Montets (1461 m a.s.l.) was free of ice before the Younger Dryas (Jaillet and Ballandras, 1999). Using ^{10}Be cosmogenic dating on the frontal moraine of the Argentière glacier confirms that the glacier was restricted to the bottom of Chamonix valley at ca. 12 ka ago (Protin et al., 2019) and lost its downslope continuity.

On the southern slopes of the ARM, small cirque glaciers were nonetheless present until the Younger Dryas (Nicoud et al., 2005) and even to approximately 8 ka ago as shown by ^{10}Be cosmogenic dating of glacial polish (Cara et al., 2017). Numerous small lakes and bogs have set up in the glacial overdeepening. Furthermore, rock glaciers and local moraines suggest that small glaciers developed during the Little Ice Age in the upper part of the two sides of the ARM. It is still glacierized above 2400 m a.s.l. with five small glaciers (< 0.1 km^2), and locally permafrost-affected rockwalls (Magnin et al., 2015). Figure 3 shows the entire study area seen from the Glacier de Lognan, on the other side of the valley.

2.3 Geology and tectonics:

The ARM is mostly composed of metamorphic rocks such as gneiss, mica schist, and granite (von Raumer, 1987) and is crossed by the active Vallorcine fault (Fig. 1). This fault is one of the major tectonic structures of the area. It extends between the Rhône River and Chamonix and regularly reactivates. The Vallorcine fault is the geological contact between the Aiguilles Rouges gneiss and the Vallorcine granite. It was presumably the seismic location of the M_w 5.3 earthquake that affected the area in 1905 (Cara et al., 2017) and the Vallorcine seismic swarm is running along the fault (Ritz et al., 2021).

The Remuaz fault (Fig. 4a) extends from the southern end of the Vallorcine fault for approximately 15 km between the Col des Montets and the Chéserys area. It is an active fault with a dominant dextral strike–slip component compatible with a tectonic origin for the postglacial deformation as suggested

by shifted glacial landforms (Ritz et al., 2021). The southern part of the Remuaz fault is oblique to the Arve valley. The southwestern end disappears under a scree on the steep slopes and possibly under sedimentary rocks in the Chamonix valley.

Several gravitational scarps have been mapped by the Bureau de Recherches Géologiques et Minières (BRGM; Pairis et al., 1992) and some have been interpreted as deep-seated RSFs by Blondeau (2018) and Blondeau et al., 2021. Furthermore, displacement rates between 2014 and 2018 were estimated over the western Alps using interferometric synthetic aperture radar (InSAR) time series from 130 Sentinel-1 acquisitions and 800 interferograms (André et al., 2021). These satellite data suggest a present-day downhill creeping in some portions of the steep slope of the ARM, but more work is needed to precisely estimate a motion value. Nonetheless, there has never been a quantitative study about the geometry of the geological objects and rates of the gravitational processes, which is the purpose of this work. To avoid the complexity related to the spatial superposition of active tectonic and gravitational features, we focus on the gravitational features located downslope of the clearly expressed part of the Remuaz fault (Fig. 4a). Our study site is located within the gneiss between the slightly flat area and the valley slope.

3. Methods

3.1 Geomorphologic and structural methods

The general strategy is based on three methods as follows: 1) A cartographic approach using aerial images acquired and orthorectified by Institut national de l'information géographique et forestière (IGN) with a resolution of 0.2 m and a high-resolution DEM from the Institut National de la Recherche Agronomique (INRAe) made by airborne LiDAR in 2012 with meter-scale resolution. 2) A visual reconnaissance from a helicopter that also allowed the acquisition of high-resolution photos that were used to make a local photogrammetric three-dimensional (3D) model using Agisoft LLC Metashape software (professional edition, version 1.8) and reached a resolution < 0.5 m (see the result here: Buoncristiani, 2020). Cross sections derived from this DEM allowed the precise

150 determination of gravitational structures' geometries. 3) Field work to determine structural
151 measurements (orientation and dip of the fractures as well as amplitude of displacement along the
152 fractures). For open fractures (called crevasses hereafter), we chose to measure the total
153 displacement vector from characteristic irregularities located both at the footwall and at the hanging
154 wall and to define this vector by its norm (total displacement measured with a laser range finder), its
155 orientation with respect to north in the horizontal plane, and its dip (Fig. 5). The total displacement is
156 composed of two distinct vertical and horizontal components. If the dip is greater than 45°, the
157 magnitude of the vertical component is greater than that of the horizontal component. Furthermore,
158 the upslope wall of the crevasse forms a clear morphological scarp if the dip of the displacement
159 vector is greater than the dip of the topographic slope (α). The crevasse's strike and dip (θ) are mean
160 values estimated from aerial photographs and field measurements. The opening is estimated in a
161 horizontal plane perpendicular to the crevasse orientation.

162 **3.2 Cosmogenic dating**

163 To constrain the timing of both glacier retreat and initiation of the RSF, we performed CRE dating
164 using *in-situ* beryllium-10 (^{10}Be). In the southern part of the ARM, the dominant lithology favored the
165 use of ^{10}Be in quartz. Sampling locations are given in Figure 4a–d and the characteristics of the
166 sampled surfaces are given in Table 1. In total, 11 rock samples of approximately 0.5 kg to 1 kg were
167 extracted. Two types of morphologies were sampled: a near-vertical scarp of gravitational origin (9
168 samples) and glacially polished surface (2 samples). The two glacially polished surfaces are located at
169 the hanging wall (AIG20-1, top of the scarp) and the footwall of the sampled gravitational scarp
170 (AIG20-7).

171 Samples were prepared at the geo-thermo-chronology (GTC) platform [Institut des Sciences de la
172 Terre (ISTerre) lab, Grenoble, France] following a procedure adapted from Brown et al. (1991) and
173 Merchel and Herpers (1999); see Appendix A. Then, ^{10}Be/^{9}Be ratios were measured at the

Accelerator Mass Spectrometry facility (ASTER), CEREGE, Aix-en-Provence, France (see Appendix A and references therein).

Exposure ages were calculated using the online CREp calculator (Martin et al., 2017). We used a global averaged time-dependent sea level high-latitude (SLHL) ^{10}Be production rate of 4.09 ± 0.19 atoms g^{-1} yr^{-1} (Martin et al., 2017). As most of the samples are from a south-exposed slope steeper than 45°, preventing the persistence of snow, ages were computed without considering snow shielding and assuming a negligible denudation. Results are presented in Table 3.

Exposure ages of samples extracted along the gravitational scarp should be considered as the maximum apparent ages because a significant inheritance may have been accumulated at depth before direct scarp exposure (e.g., Zerathe et al., 2013, 2014). Indeed, an inherited component of cosmogenic radionuclide concentration acquired before direct exposure should be considered for surface samples as well as at depth (e.g., Benavente et al., 2017; Schwartz et al., 2017; Hilger et al., 2019; Břežný et al., 2021). In the present case, the sampled gravitational scarp affects a glacially polished surface (Fig. 5) leading to a basic set of three hypotheses for inheritance calculation. 1) At the time of the glacier retreat, the polished surface is free of cosmogenic nuclides due to the previous strong ice abrasion. 2) Cosmogenic production starts on polished surface through direct exposure (t0), as well as at depth due to the penetration of high-energy particles (neutrons and then muons; Braucher et al., 2013). A large quantity of inherited nuclides can form before scarp exposure if the slip event is significantly delayed with respect to glacier retreat. 3) Finally, when the slip starts (t1), the scarp is directly exposed to cosmic rays and accumulates an additional quantity of cosmogenic nuclides. Deciphering the different steps and the ^{10}Be accumulation component is based on glacier retreat timing (t0) deduced from surface samples. An inheritance can be calculated using the classic equation (see Appendix B) used for calculation of *in-situ* cosmogenic nuclide accumulation (Lal, 1991) as described by Břežný et al. (2021) and considering an integration time t_{int} = t0 − t1 and an estimated depth, determined as follows:

199 $$Z_E = \frac{\sin\alpha \times L}{\sin\theta}, \quad (1)$$

200

201 where α is the dip of the topographic slope, *L* the distance between the sample and the top of the
202 scarp, and θ is the dip of the crevasse. Finally, this inherited ^{10}Be concentration is substracted from
203 the measured concentration (Table 3). Corrected ages are calculated as previously described using
204 the same parameters on the online CREp calculator (Martin et al., 2017).

205 **4. Results**

206 **4.1. Geomorphology and structural geology**

207 The tectonic structures are characterized by a rather planar pattern (Fig. 4a) and the Remuaz
208 fault is a subvertical fault dipping strongly to the southeast. A second fault, which we call the
209 Aiguillette fault, is trending N52° and dipping 79° to the northwest.Downslope of the Remuaz fault,
210 we have identified a rock crevasse that is several kilometers long (Fig. 4a), extending between 1700
211 and 2000 m a.s.l. The walls of the crevasse are very irregular and formed by an amalgam of different
212 fractures. In addition, some portions of these crevasses are covered by scree associated with snow
213 avalanches and boulder/rock falls from the upper cliffs (Fig. 4a–c).

214 In the northeastern part of the Argentière crevasse (Fig. 4c), downslope of the *Tête aux*
215 *Vents*, the rupture occurred upslope of a cliff where the slope changes from 78° to 35° (Fig. 5a). The
216 vertical component that moved down the downslope wall reaches 7 m (Fig. 6a) and is greater than
217 the horizontal component, as the dip of the displacement is always greater than 45° (Table 2). The
218 total displacement between the two walls reaches 13 m and is nearly parallel to the approximately
219 N100° main dip of the hillslope. As the crevasses are composed of several segments with different
220 orientations, the distances measured perpendicular to the walls and strike–slip components are
221 variable. The opening of the rock crevasse reaches 10 m where the crevasse is oriented N42°E
222 perpendicular to the displacement, whereas the opening is only 1.5 m where the crevasse is oriented

223 N164° and associated with a large strike–slip component. The cliff present in the prolongation of the
224 northeastern termination of the Argentière crevasse (Fig. 5a) probably corresponds with the footwall
225 of a now collapsed gravitational structure. Indeed, a large scree including a chaotic array of blocks—
226 some of which reach sizes greater than 10^3 m^3 (Fig. 5f)—has been fed by collapses from this area.

227 The southwestern part of the rock crevasses (Fig. 4b), located close to the Chéserys chalet, shows a
228 maximum displacement of 7.2 m (Fig. 5e) and the magnitude of the vertical component is less than
229 that of the horizontal component, with the dip of the displacement vector less than 45° (Table 2),
230 and the dip of the displacement is close to the topographic slope. At the southwestern end, the
231 motion of the crevasse system is transferred toward the north by a fracture that is nearly parallel to
232 the displacement vector and crosses the Remuaz fault (Fig. 4a). This transfer fault connects to a
233 system of several fractures on the western side of the Remuaz fault that are nearly parallel to it.
234 These fractures are less planar than the Remuaz fault and their downslope compartments are
235 lowered. Numerous fractures, parallel or perpendicular to the major crevasse, are observed. Many of
236 them are slightly open (< 1 m). The vertical motion on these open fractures is very limited (< few
237 centimeters). The use of a sounding line (thin rope with a weight) has shown depths greater than 15
238 m. The total rock volume involved is thus estimated at $5 \pm 3 \times 10^6$ m^3. The northeastern termination
239 of the Argentière crevasse is currently unstable and a diachronic analysis, based on IGN aerial
240 images, shows that an approximately 2.5×10^3 m^3 block collapsed sometime between 1949 and
241 1960.

242 **4.2. Chronological results**

243 We sampled the crevasse in the portion where the opening width is the smallest and is similar to a
244 fault scarp (site 1, Table 2). This is situated where the angle between the motion vector and the
245 fracture location is the smallest, 12° (Fig. 5c, d). ^{10}Be concentrations and related exposure ages are
246 reported in Table 3. In the following section, ages are considered with external uncertainties
247 including the uncertainty on the production rate. Exposure ages obtained from the offset surface are

17.5 ± 1.0 ka (AIG20-1) and 18.9 ± 1.0 ka (AIG20-7), for the hanging wall scarp and its footwall, respectively. These two values are indistinguishable within uncertainties and have a weighted mean of 18.2 ± 0.7 ka. This confirms the geomorphological observation that the gravitational scarp cut a glacially polished surface that is of the same age and that was initially continuous along the slope. The raw exposure ages (i.e., calculated without inheritance correction) obtained along the scarp, from the scarp top to the scarp toe, range from 3.0 ± 0.6 ka (AIG20-2) to 0.7 ± 0.3 ka ago (AIG20-6) for profile P1 and from 2.3 ± 0.4 ka (AIG20-17) to 1.0 ± 0.3 ka (AIG20-19) for profile P2 (Fig. 6). These ages should be considered as maximum exposure ages. Figure 7 shows that the age distributions of the two profiles are almost identical and that the exposure ages decrease as a function of the distance to the top scarp, except for the first sample of profile P2 (AIG20-16: 1.6 ± 0.3 ka) which is considered as outlier due to scarp rejuvenation and that is thus discarded for the following discussion. With the inheritance correction (see section 3.2), the exposure ages become much younger, ranging from 1.3 ± 0.3 to 0.6 ± 0.3 ka and from 2.0 ± 0.3 to 0.9 ± 0.3 ka, for profiles P1 and P2, respectively (Table 3). The corrected ages should be considered as minimum exposure ages.

5. DISCUSSION

5.1 A complex fracture pattern above the village of Argentière

This new structural work has clarified the geometry of the deep-seated gravitational slope deformation system located above the village of Argentière. The crevasse system does not have the same direction as the plane of the Remuaz fault (Fig. 4) and the similarly oriented Aiguillette fault dips to the northwest while the crevasse system dips to the southeast (Fig. 6). At the southwestern end, the crevasse system intersects the Remuaz fault. The amount and the dip of the displacement increase from southwest to northeast (Table 2). Currently, at the northeastern end of the Argentière crevasse, the cliff corresponds to the extension of the footwall of the crevasse that has probably been exposed by the collapse of a former block (Fig. 4c, 5a). This portion of the cliff suggests that the surface rupture does not propagate far below the surface but tends to emerge at the base of the

cliff. These observations indicate a more mature structure in the NE, and suggest a propagation of the structure to the southwest. This would suggest that the structure initiated later toward the southwest than in the portion where the chronological constraints were obtained. All these geometric characteristics suggest that the geometry of the gravity system is largely independent of the geometry of the Remuaz fault and no evidence exists to relate the crevasse development with the active fault movements.

5.2 Northeastern Argentière crevasse initiation and kinematics

The exposure ages corrected with inheritance data provide estimates for the timing of the crevasse initiation. Slip along the scarp could have occurred progressively, as corrected ages (Fig. 7b) are generally younger with depth. The standard deviations of several linear regression fits are in the order of measurement uncertainty. The least-squares regression method suggests an average slip rate of 7.6 m/ka, with standard deviations between data and linear fits that reach 0.38 ka. On the other hand, as most of the corrected exposure ages are compatible within uncertainties (Fig. 7c), an instantaneous (or very fast) event could have also occurred at a time equal to the weighted mean of 1.3 ± 0.6 ka. An instantaneous slip at 1.3 ka provides a slightly greater standard deviation of 0.45 ka. The instantaneous slip model at 1.3 ka provides a lower bound for the initiation of the crevasse.

The end of the motion would have occurred more than 0.6 ka ago based on the lowest slip rate model. This agrees with the samples located at the base of the scarp (AIG20-6 and AIG20-19) that indicate corrected exposure ages of 0.6 ± 0.3 ka and 0.9 ± 0.3 ka ago. In summary, the kinematic activity of the main crevasse would have started less than 1.3–2.5 ka ago. Furthermore, it could have been progressive and it cannot be excluded that movement is still ongoing on the main crevasse and the other crevasses located downslope. This possible present-day activity is consistent with the 2014–2018 InSAR displacement fields preliminarily estimated at a few millimeters per year below the northeastern end of the Argentière crevasse (André et al., 2021).

5.3 Time lag between gravitational failure initiation and glacier retreat

A time lag between gravitational collapse and glacier retreat has frequently been observed elsewhere, and the fundamental role of postglacial debuttressing in the initiation of gravitational structures on alpine valley flanks has been identified (Cossart et al., 2008; McColl, 2012). However, information to support this relation based on dating both the initiation of the gravity structure and the time of debuttressing of the slopes remains scarce. In the western Alps, the Tinée valley was completely deglaciated approximately ca. 13 ka ago (Bigot-Cormier et al., 2005) while the first gravitational movement of the La Clapière landslide occurred at approximately 10 ka, implying a time lag of approximately 3 ka (Bigot-Cormier et al., 2005; El Bedoui et al., 2009; Jomard et al., 2014). In the Romanche Valley (France), Le Roux et al. (2009) and Schwartz et al. (2017) found that glacier retreat at the summit scarp was achieved between ca. 17 and 13 ka ago while the landslide initiated between 8 and 6 ka ago, implying that the rupture occurred with a delay of minimum 5 ka. At Flims (Switzerland), a rockslide occurred more than 2.5 ka after deglaciation (Ivy-Ochs, 2009). In the Val Viola (Italy), the rockslide occurred more than 4 ka after deglaciation (Hormes et al., 2008). The Fernpass (Austria) rockslide occurred 1 ka after the retreat of the glacier (Prager et al., 2009a). These studies indicate that deglaciation occurred earlier than the rockslide initiation but in most cases the delay is less than 5 ka. In the present study, the time lag between the initiation of the dated scarp and the disappearance of the glacier at the level of the scarp is significantly higher, with a value reaching approximately 15 ka.

5.4 Delayed deformation models involving both debuttressing and fluid pressure

Glacial processes can be a cause of RSF initiation, although they precede the initiation by several thousand years. Mechanical modeling (Riva et al., 2018) indicates that large alpine rock slopes undergo long-term evolution in paraglacial to postglacial environments. Progressive RSFs of deglaciated slopes occur due to rock mass weakening, increased permeability, and damage linked to fluid-to-solid hydromechanical coupling. These progressive failures promote the development of

potentially catastrophic rockslides that would occur several thousands to ten thousand years after the debuttressing (Riva et al., 2018). The large time lag between initiation and gravitational activity raises the possibility of rainfall, snowmelt, or extreme meteorological events as main triggers of the gravitational activities. Ivy-Ochs et al. (2009) found that some of the largest landslides in the Alps did not occur directly after deglaciation but during the Early to Middle Holocene. They initiated close to the Preboreal/Boreal transition (approximately 10 ka ago). That is the case for Köfels (9.8 ka ago, Ivy-Ochs et al., 1998), Kandertal (9.6 ka ago, Tinner et al., 2005) and Flims (8.9 ka ago, Ivy-Ochs et al., 2009), for example. This transition is marked in Western Europe by a shift to significantly warmer and wetter conditions, with an increase of the mean temperature of 1°C to 2°C (Rasmussen et al., 2006) and heavy annual precipitations, as evidenced by lake level (Magny et al., 2011). Therefore, external hydrological parameters may have an amplifying effect on the postdebuttressing gravitational instabilities. A synthesis of all large (>10^6 m^3) rock slope instability events has been carried out across the Alps, including the nonglaciated parts (Zerathe et al., 2014, and references therein). Two temporal clusters have been identified regardless of process (including initiation/reactivation and catastrophic collapse of Sackungen, deep-seated landslides, earthflows, and rockfalls). The first cluster, between 11 and 8 ka ago, is related to paraglacial readjustment by progressive failure at the transition to the Holocene (Prager et al., 2009a,b). The second, 5 -3 ka ago (Zerathe et al., 2014), is related to seismicity (Prager et al., 2008) or paleohydrological cycles during the Middle Holocene climatic transition (Prager et al., 2008; Zerathe et al., 2014).

The initiation of the Argentière crevasse occurred during the Late Holocene, later than all the previously mentioned gravitational instabilities, and this slope failure had likely required the superposition of several factors. Topography first plays a major role in the rock slope instability. In the case of the Argentière crevasse (Fig. 8), the rupture occurred upslope of a rock wall with a slope of 78°. This topography is the result of the glacier erosion that shaped the slopes at the valley scale before the LGM. However, the very long time lag (ca. 15 ka) between the complete deglaciation, which rapidly occurred at Argentière, releasing the

entire slope between 18 and 15 ka ago (Fig. 8), and the RSF initiation (1.3 – 2.5 ka ago), reasonably exclude a direct effect of slope debuttressing here. However, it is not excluded that debuttressing could have led to previous rockfalls 15 ka ago along the valley of Chamonix as several blocks were observed along the lower slopes, but this topic would require a dedicated study. Eventually, wet climatic events, and particularly those beginning approximately 2.7 ka ago at the transition from sub-Boreal to sub-Atlantic periods (Fig. 9), may have favored the hydraulic loading of interconnected fractured areas during progressive mechanical damage. Then, a drift toward a peak of wetter conditions that is evidenced around 1.6 ka ago (Arnaud et al., 2012), as recorded in the sedimentary archives of the Bourget lake (Western Alps) (Fig. 9), may also have accelerated the failure.

Regarding the permafrost, there is no observable evidence that ice is currently present in the Argentière crevasse, and Boeckli et al. (2012) did not model permafrost at the same altitude (1900 m a.s.l.) in their Alpine Permafrost Index Map. Furthermore, Heiri et al. (2015) who used biotic proxies in lake sediments from French and Swiss Alps to reconstruct palaeotemperatures (15000-90 Cal BP), shown that mid-Holocene July air temperatures generally range between 16.5 and 17.5°C (Heiri at al., 2015). Records for the Anterne Lake (2000 m a.s.l), located less than 10 km to the northwest of the crevasse as the crow flies, show temperatures ranging from 7.5 to 11°C for the past 2 ka. Affolter et al. (2019), thanks to Milandre Cave fluid inclusion temperature record, shown that temperature anomaly for central Europe was about -5°C 12000 years ago. These elements suggest that permafrost can be excluded at the altitude of our study site. Further studies would be necessary to determine the role played by seismicity in the initiation of the Argentière crevasse.

5.5 Gravitational hazard

The gravitational structure of the Argentière crevasse constitutes a possible significant hazard for the downslope village of Argentière, as well as road and rail infrastructures. In the documents concerning the risks to the town of Chamonix–Mont-Blanc, this structure has been

identified. It has been noted that the Béchar spur constitutes a natural bund protecting the valley downslope of the northeastern Argentière crevasse (Plan de Prévention des Risques Naturels prévisibles, 2000). Modeling using Rapid mass movement simulation (RAMMS) software (Tavernier, 2020) confirms that the village of Argentière is protected by the Béchar spur for blocks < 100 m^3. Tavernier (2020) shows that a very small percentage (less than 0.3%) of modeled rocks passes the Béchar spur and reaches the first infrastructures in the valley. However, further southwest, the valley is directly exposed to possible collapses as almost 40% of the modeled rocks cross the railway line (Tavernier, 2020). Eventually, the Argentière crevasse raises questions about its cohesion and its resistance to possible seismic shocks. Two scenarios are possible: either the different units that compose it fragment and form unitary blocks, or they fall apart in a single unit. On the one hand, the mobilized volume is of a hundred cubic meter, on the other hand, several tens of thousands. If unitary blocks can be stopped by the Béchar, the collapse of blocks with greater volume ($5 \pm 3 \times 10^6$ m^3) would threaten the valley and its inhabitants.

6. Conclusion

This work describes initial research on a deep rock slope failure in the Aiguilles Rouges Nature Reserve located in the upper Chamonix valley, French Alps. It shows that a large crevasse extends for approximately 1 km in the gneiss above the village of Argentière. The total displacement, as well as the ratio of vertical to horizontal displacement component, decreases from northeast to southwest, suggesting a southwestward propagation. The rock mass located downslope of the Argentière crevasse is itself affected by numerous open fractures. The ^{10}Be dates of the escarpment at its northeastern termination suggest that the main development initiated at 1.3–2.5 ka ago and may still be ongoing. It should be stressed that the main development of this structure occurred well after the deglaciation of this area, which occurred about 18 ka ago. Other case studies focused on similar gravitational processes in the Alps demonstrated that the time lag between the initiation of RSFs and glacier retreat was in most cases less than 5 ka. Our study suggests a time lag reaching approximately 15 ka, which reasonably allow to discard this effect here. Predisposing factors (lithology, rock mass

characteristics, and geologic structures) and potential triggering factors (exceptional rainfall events, seismic activity, changes in groundwater regime) have been discussed to understand the origins of the initiation of the Argentière crevasse. Its evolution is likely to constitute a future major risk for the upper part of the Chamonix valley. Further studies on the measurement of the current deformation, the stability of this zone, and the modeling of the trajectories of the rockfalls in this area are necessary.

Author contributions

L. Courtial-Manent performed her Master's thesis on the subject, analyzed the data and wrote the paper, J.L. Mugnier led the project, worked on the tectonics aspects and wrote the paper. S. Zerathe worked on the age interpretation, the geomorphology mapping and wrote the paper, J. Carcaillet checked the quality of the geochemical processes and worked on the ^{10}Be concentrations. R. Vassallo, J.F. Buoncristiani and L. Ravanel have helped in the mapping process and in reviewing the manuscript. L. Tavernier did his first year of Master's thesis on this subject and he participated in the fieldwork to measure the displacement vectors.

Data availability

Dataset related to this article (photography and precise description of the ^{10}Be sites, three-dimensional (3D) model, etc.) can be asked to the corresponding author.

Declaration of competing interest

The authors declare that they have no known competing financial interests or personal relationships that could have appeared to influence the work reported in this paper.

Acknowledgments

This study received financial support from the program “Investissements d’Avenir, Agence nationale de la recherche (ANR), labex Observatoire des sciences de l’univers de Grenoble (OSUG): habitability in a changing word.” The authors thank Frédéric Berger and Jean-Matthieu Monnet (Institut national de la recherche agronomique, INRAe) for sharing the high-resolution Arve valley digital elevation model, the ASTER team (Georges Aumaître, Regis Braucher, Vincent Godard, Karim Keddaouche, CEREGE) for measuring the ^{10}Be concentrations. Two anonymous reviewers are acknowledged for their comments that helped to improve the manuscript.

References

Affolter, S., Häuselmann, A., Fleitmann, D., R., L. E., Cheng, H., & Leuenberger, M. (2019). Central Europe temperature constrained by speleothem fluid inclusion water isotopes over the past 14,000 years. *Science Advances*, *5*(eaav3809), 9.

André, P., Doin, M.-P., Mathey, M., Zerathe, S., Vassallo, R., & Baize, S. (2021). *Four years of InSAR time series analysis reveals an unprecedent inventory of active DSGSD in the Western Alps* [Abstract]. EGU General Assembly 2021. https://doi.org/10.5194/egusphere-egu21-12693

Arnaud, F., Révillon, S., Debret, M., Revel, M., Chapron, E., Jacob, J., Giguet-Covex, C., Poulenard, J., & Magny, M. (2012). Lake Bourget regional erosion patterns reconstruction reveals Holocene NW European Alps soil evolution and paleohydrology. *Quaternary Science Reviews*, *51*, 81–92. https://doi.org/10.1016/j.quascirev.2012.07.025

Arnold, M., Merchel, S., Bourlès, D. L., Braucher, R., Benedetti, L., Finkel, R. C., Aumaître, G., Gottdang, A., & Klein, M. (2010). The French accelerator mass spectrometry facility ASTER: Improved performance and developments. *Nuclear Instruments and Methods in Physics Research Section B: Beam Interactions with Materials and Atoms*, *268*, 1954–1959. https://doi.org/10.1016/j.nimb.2010.02.107

Ayrton, S., Barféty, J.-C., Bellière, J., Gubler, Y., & Jemelin, L. (1987). *Chamonix—Notice explicative de la feuille de Chamonix à 1/50000*. Bureau de recherches géologiques et minières.

Balco, G., Stone, J. O., Lifton, N. A., & Dunai, T. J. (2008). A complete and easily accessible means of calculating surface exposure ages or erosion rates from ^{10}Be and ^{26}Al measurements. *Quaternary Geochronology*, *3*(3), 174–195. https://doi.org/10.1016/j.quageo.2007.12.001

Ballantyne, C. K., Sandeman, G. F., Stone, J. O., & Wilson, P. (2014). Rock-slope failure following Late Pleistocene deglaciation on tectonically stable mountainous terrain. *Quaternary Science Reviews*, *86*, 144–157. https://doi.org/10.1016/j.quascirev.2013.12.021

Benavente, C., Zerathe, S., Audin, L., Hall, S. R., Robert, X., Delgado, F., Carcaillet, J., & Team, A. (2017). Active transpressional tectonics in the Andean forearc of southern Peru quantified by ^{10} Be surface exposure dating of an active fault scarp: Active Tectonics in Southern Peru. *Tectonics*, *36*, 1662–1678. https://doi.org/10.1002/2017TC004523

Bigot-Cormier, F., Braucher, R., Bourlès, D., Guglielmi, Y., Dubar, M., & Stéphan, J.-F. (2005). Chronological constraints on processes leading to large active landslides. *Earth and Planetary Science Letters*, *235*, 141–150. https://doi.org/10.1016/j.epsl.2005.03.012

Blondeau, S. (2018). *Ruptures de Versant Rocheux (RVR) à l’échelle des Alpes occidentales: Inventaire systématique, analyse spatiale, perspectives patrimoniales*. Université Lumière Lyon 2.

464 Blondeau, S., Gunnell, Y., & Jarman, D. (2021). Rock slope failure in the Western Alps: A first
465 comprehensive inventory and spatial analysis. *Geomorphology*, *380*, 1–31.
466 https://doi.org/10.1016/j.geomorph.2021.107622
467 Boeckli, L., Brenning, A., Gruber, S., & Noetzli, J. (2012). Permafrost distribution in the European Alps:
468 Calculation and evaluation of an index map and summary statistics. *The Cryosphere*, *6*, 807–
469 820. https://doi.org/10.5194/tc-6-807-2012
470 Böhme, M., Hermanns, R. L., Gosse, J., Hilger, P., Eiken, T., Lauknes, T. R., & Dehls, J. F. (2019).
471 Comparison of monitoring data with paleo–slip rates: Cosmogenic nuclide dating detects
472 acceleration of a rockslide. Geology, 47(4), 339-342.
473 Braucher, R., Bourlès, D., Merchel, S., Vidal Romani, J., Fernadez-Mosquera, D., Marti, K., Léanni, L.,
474 Chauvet, F., Arnold, M., Aumaître, G., & Keddadouche, K. (2013). Determination of muon
475 attenuation lengths in depth profiles from in situ produced cosmogenic nuclides. *Nuclear*
476 *Instruments and Methods in Physics Research Section B: Beam Interactions with Materials*
477 *and Atoms*, *294*, 484–490. https://doi.org/10.1016/j.nimb.2012.05.023
478 Braucher, R., Guillou, V., Bourlès, D. L., Arnold, M., Aumaître, G., Keddadouche, K., & Nottoli, E.
479 (2015). Preparation of ASTER in-house $^{10}Be/^{9}Be$ standard solutions. *Nuclear Instruments and*
480 *Methods in Physics Research Section B: Beam Interactions with Materials and Atoms*, *361*,
481 335–340. https://doi.org/10.1016/j.nimb.2015.06.012
482 Braucher, R., Merchel, S., Borgomano, J., & Bourlès, D. L. (2011). Production of cosmogenic
483 radionuclides at great depth: A multi element approach. *Earth and Planetary Science Letters*,
484 *309*, 1–9. https://doi.org/10.1016/j.epsl.2011.06.036
485 Břežný, M., Pánek, T., Braucher, R., Šilhán, K., Chalupa, V., Lenart, J., Tábořík, P., & Team, A. (2021).
486 Old but still active: > 18 ka history of rock slope failures affecting a flysch anticline.
487 *Landslides*, *18*, 89–104. https://doi.org/10.1007/s10346-020-01483-7
488 Brideau, M.-A., Yan, M., & Stead, D. (2009). The role of tectonic damage and brittle rock fracture in
489 the development of large rock slope failures. *Geomorphology*, *103*, 30–49.
490 https://doi.org/10.1016/j.geomorph.2008.04.010
491 Brown, E. T., Edmond, J. M., Raisbeck, G. M., Yiou, F., Kurz, M. D., & Brook', E. J. (1991). Examination
492 of surface exposure ages of Antarctic moraines using in situ produced ^{10}Be and ^{26}A.
493 *Geochimica et Cosmochimica Acta*, *55*, 2269–2283.
494 Buoncristiani, J.-F. (2020). *Rémuaz* [Sketchfab]. https://sketchfab.com/3d-models/remuaz-
495 c17b02c34b654405a2c10fc94b9d5513
496 Cara, M., Van der Woerd, J., Alasset, P.-J., Benjumea, J., & Mériaux, A.-S. (2017). The 1905 Chamonix
497 earthquakes: Active tectonics in the Mont Blanc and Aiguilles Rouges massifs. *Swiss Journal*
498 *of Geosciences*, *110*, 631–651. https://doi.org/10.1007/s00015-017-0262-7
499 Chen, R.-F., Chan, Y.-C., Angelier, J., Hu, J.-C., Huang, C., Chang, K.-J., & Shih, T.-Y. (2005). Large
500 earthquake-triggered landslides and mountain belt erosion: The Tsaoling case, Taiwan.
501 *Comptes Rendus Geoscience*, *337*, 1164–1172. https://doi.org/10.1016/j.crte.2005.04.017
502 Chmeleff, J., von Blanckenburg, F., Kossert, K., & Jakob, D. (2010). Determination of the ^{10}Be half-life
503 by multicollector ICP-MS and liquid scintillation counting. *Nuclear Instruments and Methods*
504 *in Physics Research B*, *268*, 192–199. https://doi.org/10.1016/j.nimb.2009.09.012
505 Clark, P. U., Dyke, A. S., Shakun, J. D., Carlson, A. E., Clark, J., Wohlfarth, B., Mitrovica, J. X., Hostetler,
506 S. W., & McCabe, A. M. (2009). The Last Glacial Maximum. *Science*, *325*, 710–714.
507 https://doi.org/10.1126/science.1172873
508 Cossart, E., Braucher, R., Fort, M., Bourlès, D. L., & Carcaillet, J. (2008). Slope instability in relation to
509 glacial debuttressing in alpine areas (Upper Durance catchment, southeastern France):
510 Evidence from field data and ^{10}Be cosmic ray exposure ages. *Geomorphology*, *95*, 3–26.
511 https://doi.org/10.1016/j.geomorph.2006.12.022
512 Coutterand, S. (2010). *Étude géomophologique des flux glaciaires dans les Alpes nord-occidentales au*
513 *Pléistocène récent. Du maximum de la dernière glaciation aux premières étapes de la*
514 *déglaciation*. Université de Savoie.
515 Coutterand, S., & Buoncristiani, J.-F. (2006). Paléogéographie du dernier maximum glaciaire du

Pléistocène récent de la région du Massif du Mont Blanc, France. *Quaternaire*, *17*(1), 35–43. https://doi.org/10.4000/quaternaire.633

Crosta, G. B., Frattini, P., & Agliardi, F. (2013). Deep seated gravitational slope deformations in the European Alps. *Tectonophysics*, *605*, 13–33. https://doi.org/10.1016/j.tecto.2013.04.028

Delgado, F., Zerathe, S., Audin, L., Schwartz, S., Benavente, C., Carcaillet, J., ... & Team, A. (2020). Giant landslide triggerings and paleoprecipitations in the Central Western Andes: The aricota rockslide dam (South Peru). Geomorphology, 350, 106932.

Dunne, J., Elmore, D., & Muzikar, P. (1999). Scaling factors for the rates of production of cosmogenic nuclides for geometric shielding and attenuation at depth on sloped surfaces. *Geomorphology*, 3–11.

Eberhardt, E., Stead, D., & Coggan, J. S. (2004). Numerical analysis of initiation and progressive failure in natural rock slopes—The 1991 Randa rockslide. *International Journal of Rock Mechanics and Mining Sciences*, *41*, 69–87. https://doi.org/10.1016/S1365-1609(03)00076-5

El Bedoui, S., Guglielmi, Y., Lebourg, T., & Pérez, J.-L. (2009). Deep-seated failure propagation in a fractured rock slope over 10,000 years: The La Clapière slope, the south-eastern French Alps. *Geomorphology*, *105*, 232–238. https://doi.org/10.1016/j.geomorph.2008.09.025

Guzzetti, F., Cardinali, M., Reichenbach, P., Cipolla, F., Sebastiani, C., Galli, M., & Salvati, P. (2004). Landslides triggered by the 23 November 2000 rainfall event in the Imperia Province, Western Liguria, Italy. *Engineering Geology*, *73*, 229–245. https://doi.org/10.1016/j.enggeo.2004.01.006

Harbor, J. M., Hallet, B., & Raymond, C. F. (1988). A numerical model of landform development by glacial erosion. *Nature*, *333*, 347–349.

Heiri, O., Ilyashuk, B., Millet, L., Samartin, S., & Lotter, A. F. (2015). Stacking of discontinuous regional palaeoclimate records: Chironomid-based summer temperatures from the Alpine region. *The Holocene*, *25*(1), 137–149. https://doi.org/DOI: 10.1177/0959683614556382

Herman, F., Beaud, F., Champagnac, J.-D., Lemieux, J.-M., & Sternai, P. (2011). Glacial hydrology and erosion patterns: A mechanism for carving glacial valleys. *Earth and Planetary Science Letters*, *310*, 498–508. https://doi.org/10.1016/j.epsl.2011.08.022

Hilger, P., Gosse, J. C., & Hermanns, R. L. (2019). How significant is inheritance when dating rockslide boulders with terrestrial cosmogenic nuclide dating?—A case study of an historic event. *Landslides*, *16*, 729–738. https://doi.org/10.1007/s10346-018-01132-0

Holm, K., Bovis, M., & Jakob, M. (2004). The landslide response of alpine basins to post-Little Ice Age glacial thinning and retreat in southwestern British Columbia. *Geomorphology*, *57*, 201–216. https://doi.org/10.1016/S0169-555X(03)00103-X

Hormes, A., Ivy-Ochs, S., Kubik, P. W., Ferreli, L., & Maria Michetti, A. (2008). ^{10}Be exposure ages of a rock avalanche and a late glacial moraine in Alta Valtellina, Italian Alps. *Quaternary International*, *190*, 136–145. https://doi.org/10.1016/j.quaint.2007.06.036

Ivy-Ochs, S., Heuberger, H., Kubik, P. W., Bonani, G., Franck, M., & Schlüchter, C. (1998). The age of the Köfels event: Relative, ^{14}C and cosmogenic isotope dating of an early Holocene landslide in the Central Alps (Tyrol, Austria). *Z. Gletsch.Kd. Glazialgeol.*, *34*, 57–68.

Ivy-Ochs, S., Poschinger, A. v., Synal, H.-A., & Maisch, M. (2009). Surface exposure dating of the Flims landslide, Graubünden, Switzerland. *Geomorphology*, *103*, 104–112. https://doi.org/10.1016/j.geomorph.2007.10.024

Jaillet, S., & Ballandras, S. (1999). La transition Tardiglaciaire/Holocène à travers les fluctuations du glacier du Tour (Vallée de Chamonix, Alpes du Nord françaises) [Lateglacial/Holocene transition through glacier du Tour fluctuations (upper Chamonix valley, French Alps)]. *Quaternaire*, *10*, 15–23. https://doi.org/10.3406/quate.1999.1625

Janjou, D. (2004). *Descriptif des cartes géologiques à 1/50 000 format "vecteurs". BRGM/RP-53473-FR* (p. 21).

Jibson, R. W., Harp, E. L., Schulz, W., & Keefer, D. K. (2006). Large rock avalanches triggered by the M 7.9 Denali Fault, Alaska, earthquake of 3 November 2002. *Engineering Geology*, *83*, 144–160. https://doi.org/10.1016/j.enggeo.2005.06.029

Jomard, H., Lebourg, Th., & Guglielmi, Y. (2014). Morphological analysis of deep-seated gravitational slope deformation (DSGSD) in the western part of the Argentera massif. A morpho-tectonic control? *Landslides*, *11*, 107–117. https://doi.org/10.1007/s10346-013-0434-0

Korschinek, G., Bergmaier, A., Faestermann, T., Gerstmann, U. C., Knie, K., Rugel, G., Wallner, A., Dillmann, I., Dollinger, G., von Gostomski, Ch. L., Kossert, K., Maiti, M., Poutivtsev, M., & Remmert, A. (2010). A new value for the half-life of 10Be by Heavy-Ion Elastic Recoil Detection and liquid scintillation counting. *Nuclear Instruments and Methods in Physics Research B*, *268*, 187–191. https://doi.org/10.1016/j.nimb.2009.09.020

Lal, D. (1991). Cosmic ray labeling of erosion surfaces: In situ nuclide production rates and erosion models. *Earth and Planetary Science Letters*, *104*, 424–439.

Le Roux, O., Schwartz, S., Gamond, J. F., Jongmans, D., Bourles, D., Braucher, R., Mahaney, W., Carcaillet, J., & Leanni, L. (2009). CRE dating on the head scarp of a major landslide (Séchilienne, French Alps), age constraints on Holocene kinematics. *Earth and Planetary Science Letters*, *280*, 236–245. https://doi.org/10.1016/j.epsl.2009.01.034

Lehmann, B., Herman, F., Valla, P. G., King, G. E., Biswas, R. H., Ivy-Ochs, S., Steinemann, O., & Christl, M. (2020). Postglacial erosion of bedrock surfaces and deglaciation timing: New insights from the Mont Blanc massif (western Alps). *Geology*, *48*(2), 139–144. https://doi.org/10.1130/G46585.1

Lifton, N. (2016). Implications of two Holocene time-dependent geomagnetic models for cosmogenic nuclide production rate scaling. *Earth and Planetary Science Letters*, *433*, 257–268. https://doi.org/10.1016/j.epsl.2015.11.006

Magnin, F., Brenning, A., Bodin, X., Deline, P., & Ravanel, L. (2015). Modélisation statistique de la distribution du permafrost de paroi: Application au massif du Mont Blanc. *Géomorphologie : Relief, Processus, Environnement*, *21*(2), 145–162. https://doi.org/10.4000/geomorphologie.10965

Magny, M., Bossuet, G., Ruffaldi, P., Leroux, A., & Mouthon, J. (2011). Orbital imprint on Holocene palaeohydrological variations in west-central Europe as reflected by lake-level changes at Cerin (Jura Mountains, eastern France). *Journal of Quaternary Science*, *26*(2), 171–177. https://doi.org/10.1002/jqs.1436

Martin, L. C. P., Blard, P.-H., Balco, G., Lavé, J., Delunel, R., Lifton, N., & Laurent, V. (2017). The CREp program and the ICE-D production rate calibration database: A fully parameterizable and updated online tool to compute cosmic-ray exposure ages. *Quaternary Geochronology*, *38*, 25–49. https://doi.org/10.1016/j.quageo.2016.11.006

McColl, S. T. (2012). Paraglacial rock-slope stability. *Geomorphology*, *153–154*, 1–16. https://doi.org/10.1016/j.geomorph.2012.02.015

Merchel, S., & Herpers, U. (1999). An Update on Radiochemical Separation Techniques for the Determination of Long-Lived Radionuclides via Accelerator Mass Spectrometry. *Radiochimica Acta*, *84*, 215–219. https://doi.org/10.1524/ract.1999.84.4.215

Nicoud, G., Coutterand, S., & Moreau, L. (2005). Arrêt 4 -L'ombilic de Chamonix—Les Houches (Les Bossons). *Collection EDYTEM. Cahiers de Géographie*, *3*(1), 40–46. https://doi.org/10.3406/edyte.2005.913

Nishiizumi, K., Winterer, E. L., Kohl, C. P., Klein, J., Middleton, R., Lal, D., & Arnold, J. R. (1989). Cosmic ray production rates of ^{10}Be and ^{26}Al in quartz from glacially polished rocks. *Journal of Geophysical Research*, *94*(B12), 17907–17915. https://doi.org/10.1029/JB094iB12p17907

Office National des Forêts, Service de Restauration des Terrains en Montagne, Direction Départementale de l'Agriculture et de la Forêt, & Préfecture de la Haute-Savoie. (2000). *P.P.R Révision Partielle du Plan de Prévention des Risques Naturels Prévisibles. Commune de Chamonix Mont-Blanc—Rapport de présentation.*

Pánek, T. (2015). Recent progress in landslide dating: a global overview. Progress in Physical Geography, 39(2), 168-198.

Pánek, T., & Klimeš, J. (2016). Temporal behavior of deep-seated gravitational slope deformations: A review. Earth-Science Reviews, 156, 14-38.

Pairis, J. L., Bellière, J., & Rosset, J. (1992). *Notice explicative de la feuille Cluses à 1/50000.* (Bureau Des Recherches Géologiques et Minières, p. 89).

Pairis, J. L., Pairis, B., Bellière, J., Rosset, J., Détraz, H., Muller, A., Muller, D., Villars, F., Mennessier, G., Charollais, J., Kindler, P., Pierre, X., & Uselle, J. P. (1992). *Carte géologique de la France (1/50000), feuille Cluses* [Carte géologique]. Bureau de recherches géologiques et minières.

Pisani, G., Castelli, M., & Scavia, C. (2010). Hydrogeological model and hydraulic behaviour of a large landslide in the Italian Western Alps. *Natural Hazards and Earth System Sciences*, *10*, 2391–2406. https://doi.org/10.5194/nhess-10-2391-2010

Pothérat, P., & Effendiantz, L. (2009). Néotectonique et grands mouvements de versant. Le cas de Séchilienne (Isère, France). *Bulletin of Engineering Geology and the Environment*, *68*, 567–577. https://doi.org/10.1007/s10064-009-0221-2

Prager, C., Ivy-Ochs, S., Ostermann, M., Synal, H.-A., & Patzelt, G. (2009b). Geology and radiometric ^{14}C-, ^{36}Cl- and Th-/U-dating of the Fernpass rockslide (Tyrol, Austria). *Geomorphology*, *103*, 93–103. https://doi.org/10.1016/j.geomorph.2007.10.018

Prager, C., Zangerl, C., & Nagler, T. (2009a). Geological controls on slope deformations in the Köfels rockslide area (Tyrol, Austria). *Austrian Journal of Earth Sciences*, *102*, 4–19.

Prager, C., Zangerl, C., Patzelt, G., & Brandner, R. (2008). Age distribution of fossil landslides in the Tyrol (Austria) and its surrounding areas. *Natural Hazards and Earth System Sciences*, *8*, 377–407. https://doi.org/10.5194/nhess-8-377-2008

Protin, M., Schimmelpfennig, I., Mugnier, J.-L., Ravanel, L., Le Roy, M., Deline, P., Favier, V., Buoncristiani, J.-F., Aumaître, G., Bourlès, D. L., & Keddadouche, K. (2019). Climatic reconstruction for the Younger Dryas/Early Holocene transition and the Little Ice Age based on paleo-extents of Argentière glacier (French Alps). *Quaternary Science Reviews*, *221*, 1–15. https://doi.org/10.1016/j.quascirev.2019.105863

Rasmussen, S. O., Andersen, K. K., Svensson, A. M., Steffensen, J. P., Vinther, B. M., Clausen, H. B., Siggaard-Andersen, M.-L., Johnsen, S. J., Larsen, L. B., Dahl-Jensen, D., Bigler, M., Röthlisberger, R., Fischer, H., Goto-Azuma, K., Hansson, M. E., & Ruth, U. (2006). A new Greenland ice core chronology for the last glacial termination. *Journal of Geophysical Research*, *111*, 1–16. https://doi.org/10.1029/2005JD006079

Ravanel, L., & Deline, P. (2011). Climate influence on rockfalls in high-Alpine steep rockwalls: The north side of the Aiguilles de Chamonix (Mont Blanc massif) since the end of the 'Little Ice Age.' *The Holocene*, *21*(2), 357–365. https://doi.org/10.1177/0959683610374887

RGI Consortium. (2017). *Randolph Glacier Inventory – A Dataset of Global Glacier Outlines: Version 6.0: Technical Report, Global Land Ice Measurements from Space, Colorado, USA. Digital Media.* https://doi.org/10.7265/N5-RGI-60

Ritz, J.-F., Baize, S., Audin, L., Authemayou, C., Kaub, C., Lacan, P., Larroque, C., Leclerc, F., Manchuel, K., Mugnier, J.-L., Ortuño, M., Rizza, M., Vassallo, R., Arroucou, P., Billant, J., Bollinger, L., Ferry, M., Fillon, C., Geoffroy, L., Jomard H., Le Roy P., Migeon S., Perrin C., Perrot J., Ratzov G., Reichter K., Soubigou O., Vergniault C., Viaplana M., Van der Woerd, J. (2021). New perspectives in studying active faults in metropolitan France: the "Active faults France" (FACT/ATS) research axis from the Resif-Epos consortium. *Compte Rendus. Géosciences, 353*, 381-412.

Riva, F., Agliardi, F., Amitrano, D., & Crosta, G. B. (2018). Damage-Based Time-Dependent Modeling of Paraglacial to Postglacial Progressive Failure of Large Rock Slopes. *Journal of Geophysical Research: Earth Surface*, *123*, 124–141. https://doi.org/10.1002/2017JF004423

Schwartz, S., Zerathe, S., Jongmans, D., Baillet, L., Carcaillet, J., Audin, L., Dumont, T., Bourlès, D., Braucher, R., & Lebrouc, V. (2017). Cosmic ray exposure dating on the large landslide of Séchilienne (Western Alps): A synthesis to constrain slope evolution. *Geomorphology*, *278*, 329–344. https://doi.org/10.1016/j.geomorph.2016.11.014

Sepúlveda, S. A., Moreiras, S. M., Chacón, D., Villaseñor, T., Jeanneret, P., & Poblete, F. (2022). The Pangal landslide complex, Cachapoal basin, central Chile (34° S): An example of a multi-temporal slope instability cluster in the Andes. Journal of South American Earth Sciences,

115, 103769.
Stone, J. O. (2000). Air pressure and cosmogenic isotope production. *Journal of Geophysical Research*, *105*(B10), 23753–23759. https://doi.org/10.1029/2000JB900181
Tavernier, L. (2020). *Etude structurale et trajectographique de la rupture de versant rocheux des Cheserys* (p. 40) [Rapport de master 1]. Université Savoie Mont Blanc.
Tinner, W., Kaltenrieder, P., Soom, M., Zwahlen, P., Schmidhalter, M., Boschetti, A., & Schlüchter, C. (2005). The postglacial rockfall in the Kander valley (Switzerland): Age and effects on palaeo-environments. *Eclogae Geologicae Helvetiae*, *98*, 83–95.
von Raumer, J. F. (1987). Les massifs du Mont Blanc et des Aiguilles Rouges: Témoins de la formation de la croûte varisque dans les Alpes occidentales. *Géologie Alpine*, *63*, 7–28.
Zeng, Q., Yuan, G., Davies, T., Xu, B., Wei, R., Xue, X., & Zhang, L. (2020). 10Be dating and seismic origin of Luanshibao rock avalanche in SE Tibetan Plateau and implications on Litang active fault. Landslides, 17(5), 1091-1104.Zerathe, S., Braucher, R., Lebourg, T., Bourlès, D., Manetti, M., & Léanni, L. (2013). Dating chert (diagenetic silica) using *in-situ* produced ^{10}Be: Possible complications revealed through a comparison with ^{36}Cl applied to coexisting limestone. *Quaternary Geochronology*, *17*, 81–93. https://doi.org/10.1016/j.quageo.2013.01.003
Zerathe, S., Lebourg, T., Braucher, R., & Bourlès, D. (2014). Mid-Holocene cluster of large-scale landslides revealed in the Southwestern Alps by ^{36}Cl dating. Insight on an Alpine-scale landslide activity. *Quaternary Science Reviews*, *90*, 106–127. https://doi.org/10.1016/j.quascirev.2014.02.015

Figure captions

Figure 1. Geological context of the studied area with shaded 75 m Digital Elevation Model (source: Institut national de l'information géographique et forestière, IGN). Altitudes are in m a.s.l. Faults and geology are based on the Bureau de Recherches Géologiques et Minières (BRGM) mapping (Pairis et al., 1992a; Pairis et al., 1992b, Janjou, 2004). Northings and eastings are according to RGF93/Lambert-93 grids. Black dashed lines represent Last Glacial Maximum glacial upper limits (Coutterand & Buoncristiani, 2006; Coutterand, 2010). Glacier extents are from the Randolph Glacier Inventory (RGI Consortium, 2017) 6.0.

Figure 2. Photo of the Aiguillette d'Argentière, famous rock-climbing site.

Figure 3. Photograph of the entire mountain slope taken from the Glacier de Lognan, on the opposite side of the Arve valley.

Figure 4. a) Geomorphologic settings of the study area showing the main structural and gravitational features. Slope map with inverse symbology (flattest slopes in white and highest in black, threshold set at 55°) derived from the Digital Elevation Model of the Institut National de la Recherche Agronomique (INRAe) 1 m high-resolution LiDAR . Slopes range from 0° to 87°. b) Zoom in on the southwestern part of the crevasse. c) Zoom in on the northeastern part of the crevasse. Numbers refer to the location of studied sites described in Table 2. Black lines correspond to the profiles through the northeastern termination of the Argentière crevasse, see Fig. 6.

Figure 5. a) Global view of the northeastern Argentière rock crevasse. b) Location of the glacially polished surface sample (AIG20-7). c) Sample location for the profile P2 (red dots). d) Sample location for the profile P1 (black dots ad blue triangle). e) Rock crevasse in the southwestern part of the structure. The displacement vector is estimated by fitting the characteristic shapes of one wall to the other. f) Collapsed rock from the northeastern part of the rock failure. Its estimated volume is greater than 1000 m^3.

Figure 6. Profiles through the eastern termination of the crevasse and location of the samples. The red dotted lines indicate the potential surfaces before the scarp development. The red dashed lines indicate the crevasses. *Location of sample AIG20-7 has been projected. The profiles were extracted from the photogrammetric three-dimensional (3D) model.

Figure 7. Plot of the ^{10}Be exposure ages as a function of the distance from the top of the scarp. a) All the obtained ages without inheritance correction. B) Corrected ages of the scarp considering inheritance before the initiation of the RSF. C) Probability density plot of the corrected ages where

731 thin black lines are individual ages (sample AIG20-16 in dashed line as outlier) and the thick blue line
732 is the summed probability curve (AIG20-16 excluded).

733 Figure 8. Section through the upper Arve valley illustrating the position of the eastern end of the
734 large crevasse in relation to the tectonic structures and the evolution of the deglaciation. (1) From
735 Coutterand and Buoncristiani (2006); (2) from this study; (3) from Jaillet and Ballandras (1999); (4)
736 from Protin et al. (2019).

737

738 Figure 9. Sedimentation rate and terrigenous contribution in the Lac du Bourget (from Arnaud et al.,
739 2012)

740

741

742 **Table captions**

743 Table 1. Sample characteristics. T is the sample thickness; Z is the distance of the sample from the
744 top of the scarp; Z_E corresponds to the estimated depth before the scarp was exhumed; S is the
745 shielding; and M_{Quartz} is the quartz mass.

746 Table 2. Structural characteristics of the main crevasses from northeast to northwest (site locations
747 shown in Fig. 4).

748 Table 3. ^{10}Be concentrations, calculated and corrected ages considering inheritance. Internal
749 uncertainty corresponds to the 1σ uncertainty without production rate errors. The in-house standard
750 (Braucher et al., 2015) and accelerator mass spectrometer internal error (0.5%; Arnold et al., 2010)
751 have been included. A blank value with a ^{10}Be/^{9}Be ratio of 6.95×10^{-15} was used to correct the
752 samples.

Figure1

Click here to access/download;Figure;Fig1_L_Courtial_Manent_revised2.png

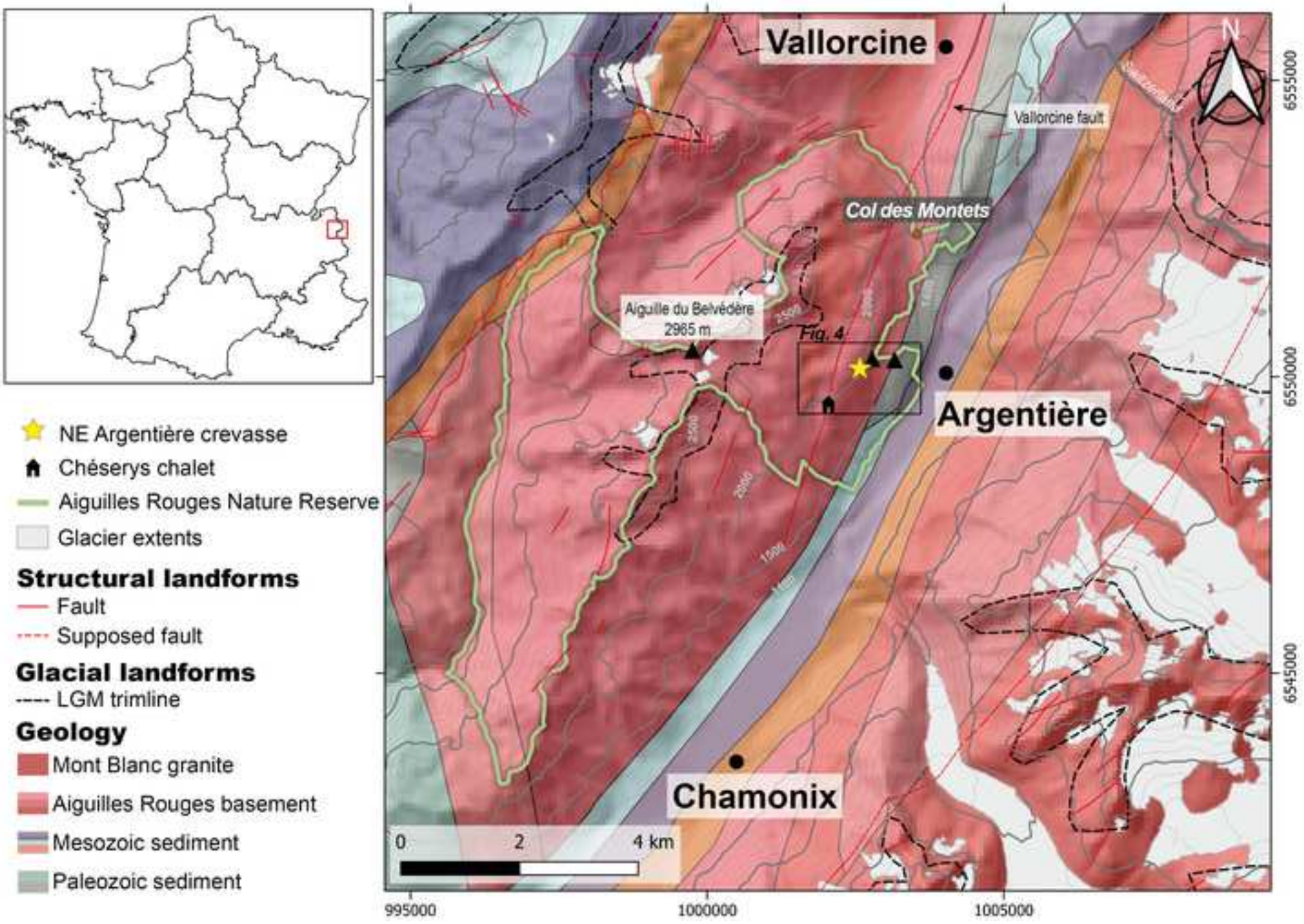

Figure2

Click here to access/download;Figure;Fig2_L_Courtial_Manent_Aiguillette.JPG

Figure3

Click here to access/download;Figure;Fig3__L_Courtial_Manent_ARM.png

Figure4a

Click here to access/download;Figure;Fig4a_L_Courtial_Manent_revised2.png

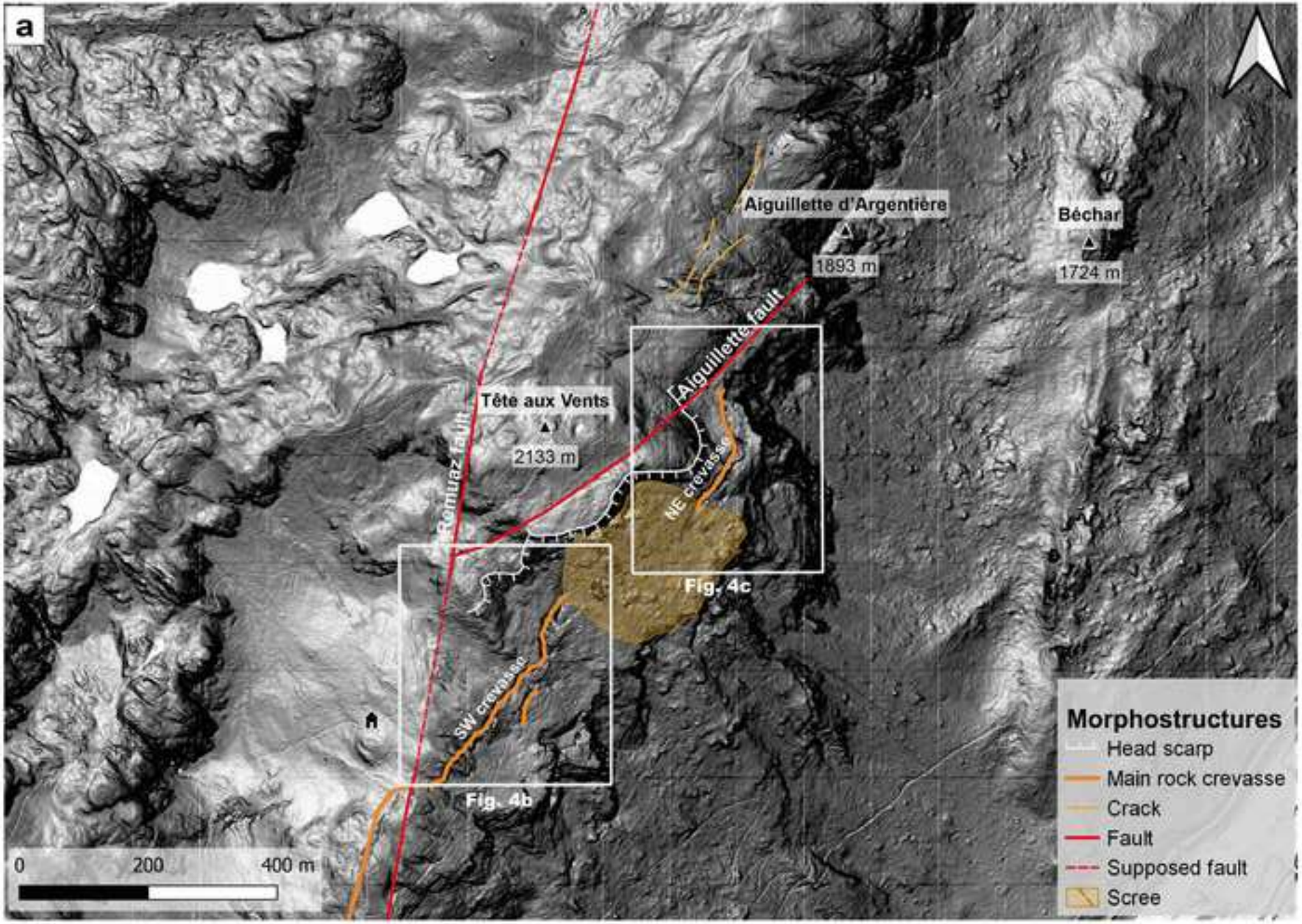

Figure4b-c

Click here to access/download;Figure;Fig4b_c_L_Courtial_Manent.png

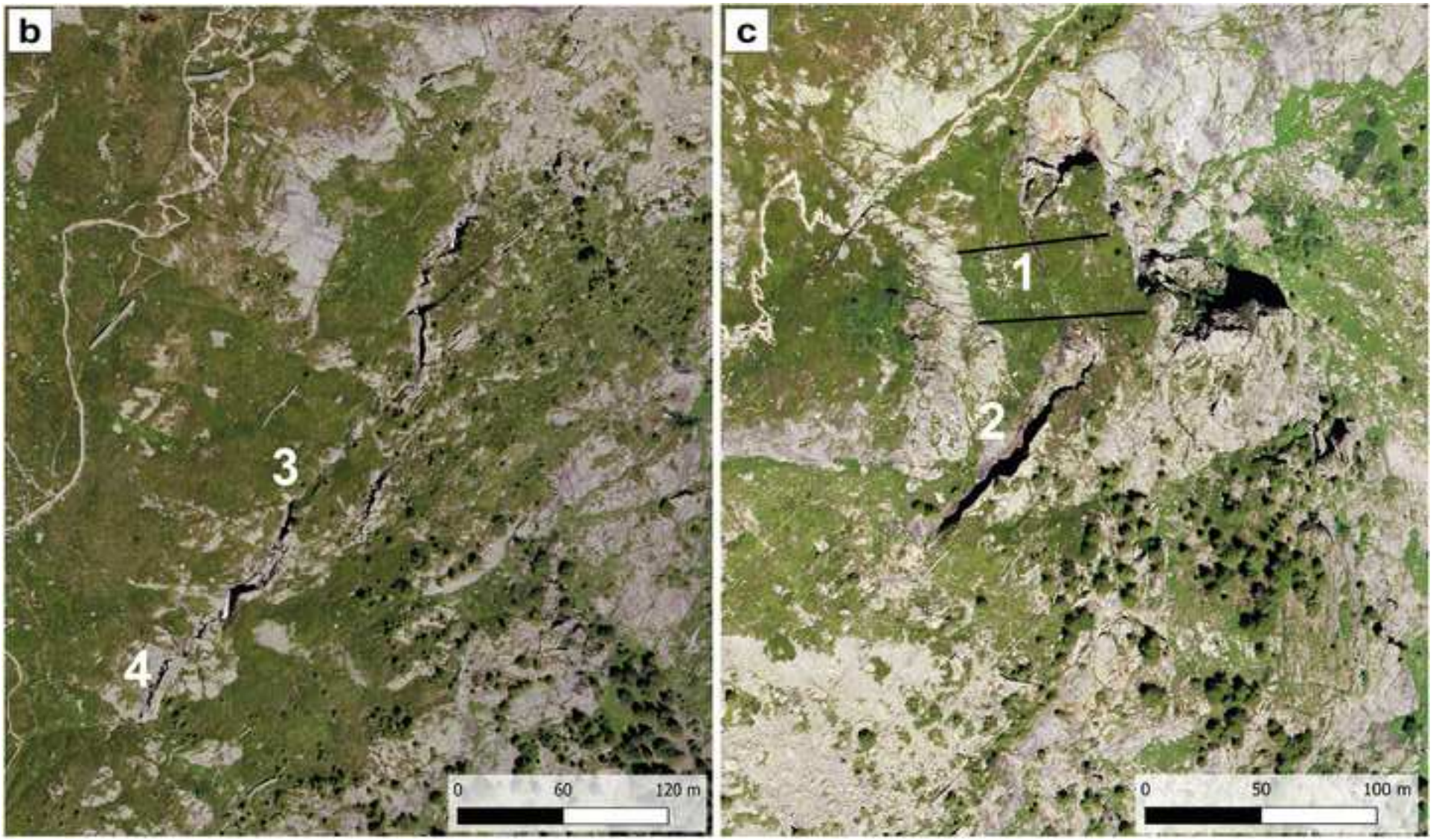

Figure5

Click here to access/download;Figure;Fig5_L_Courtial_Manent_revised.png

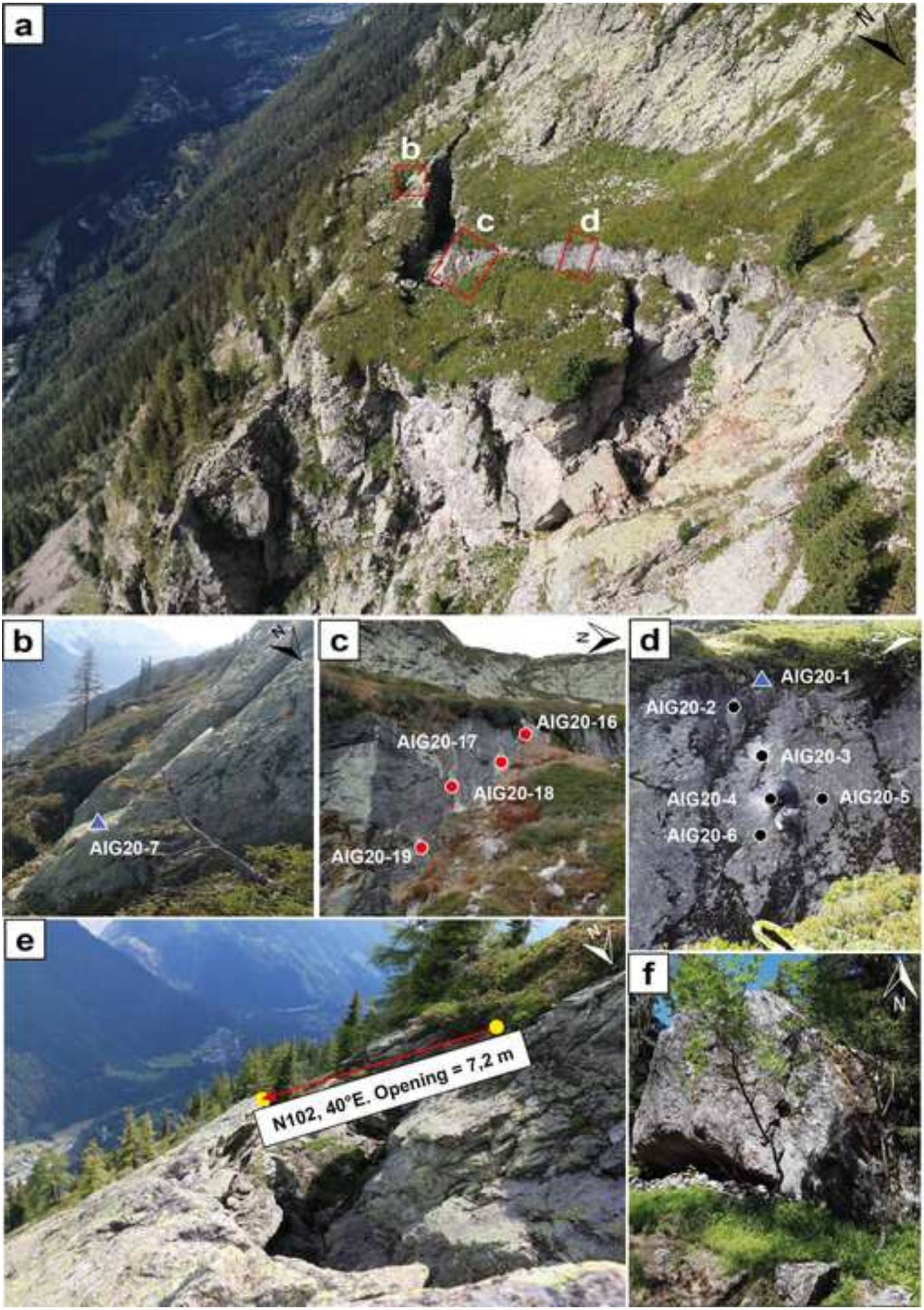

Figure6a

Click here to access/download;Figure;Fig6a_L_Courtial_Manent_revised.png

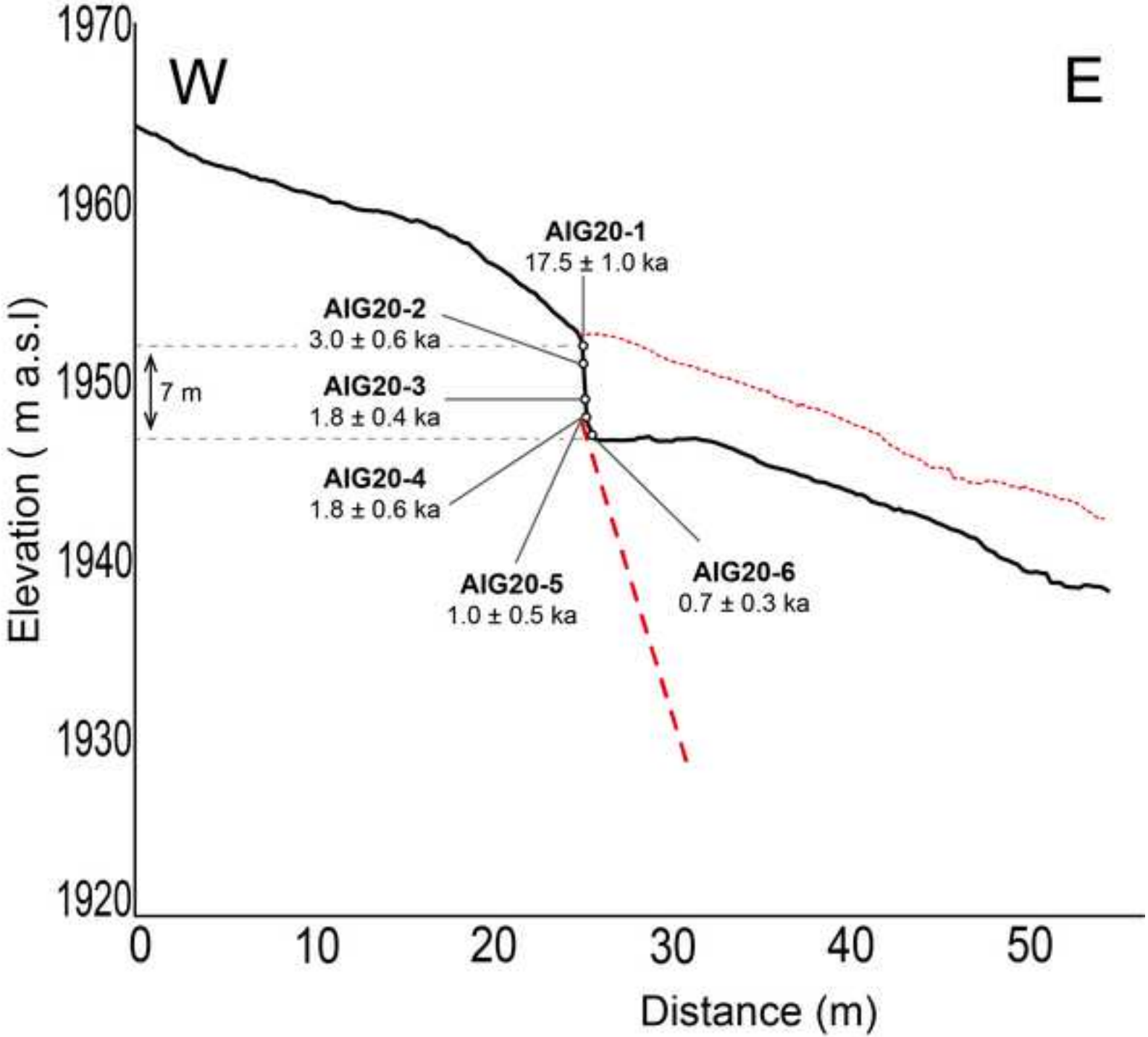

Figure6b

Click here to access/download;Figure;Fig6b_L_Courtial_Manent.png

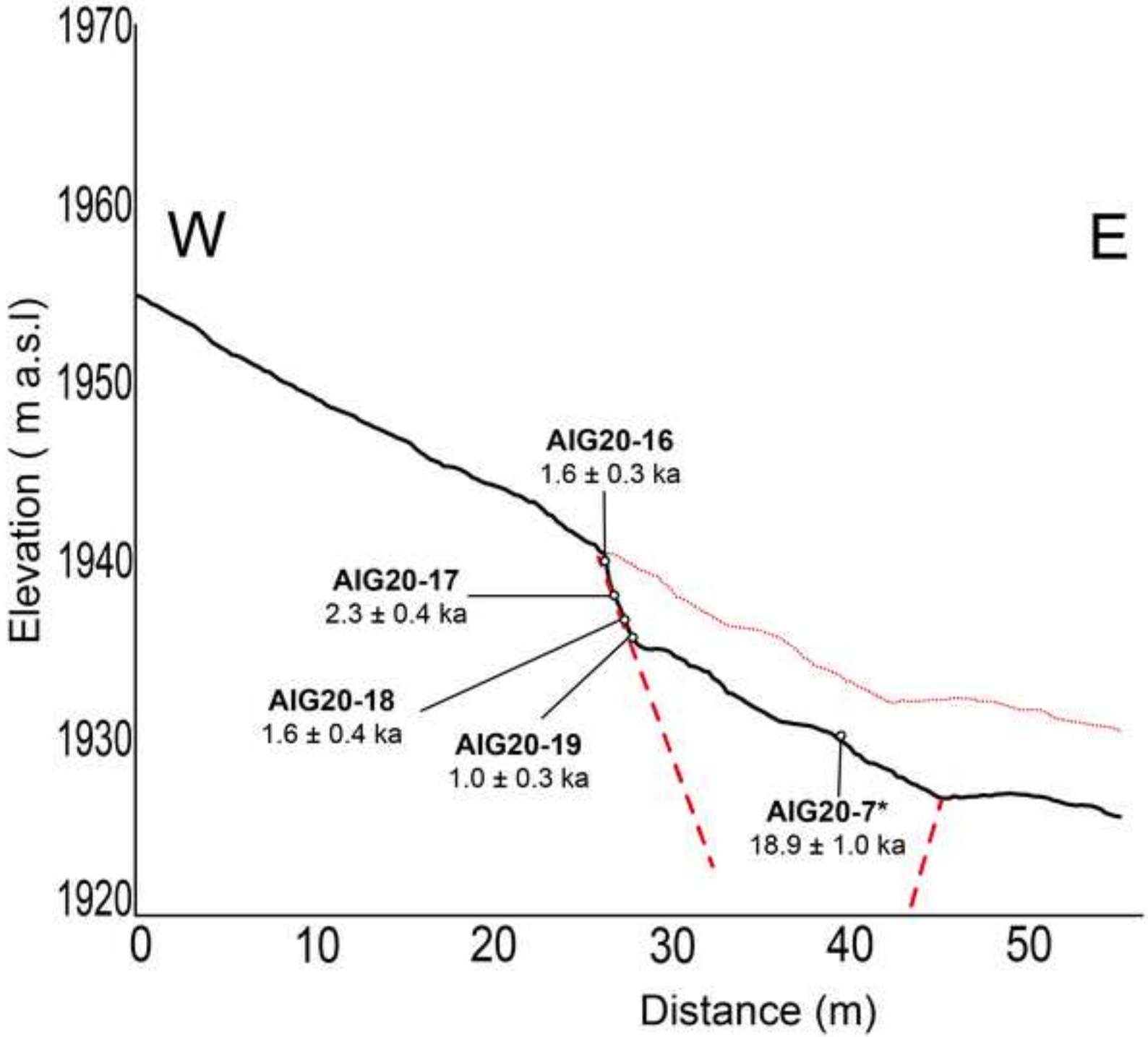

Figure7

Click here to access/download;Figure;Fig7_L_Courtial_Manent.jpg

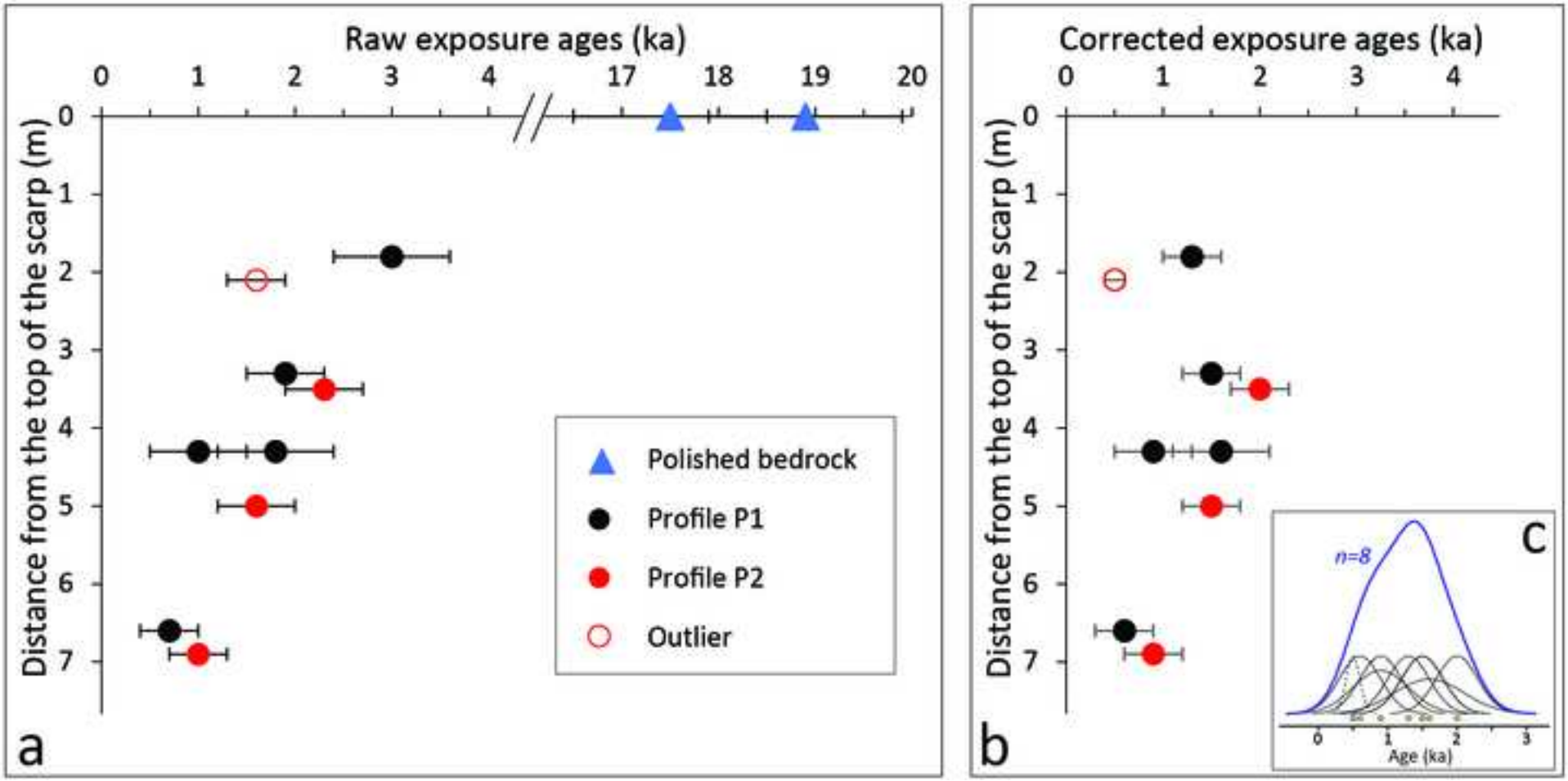

Figure8

Click here to access/download;Figure;Fig8_L_Courtial_Manent.png

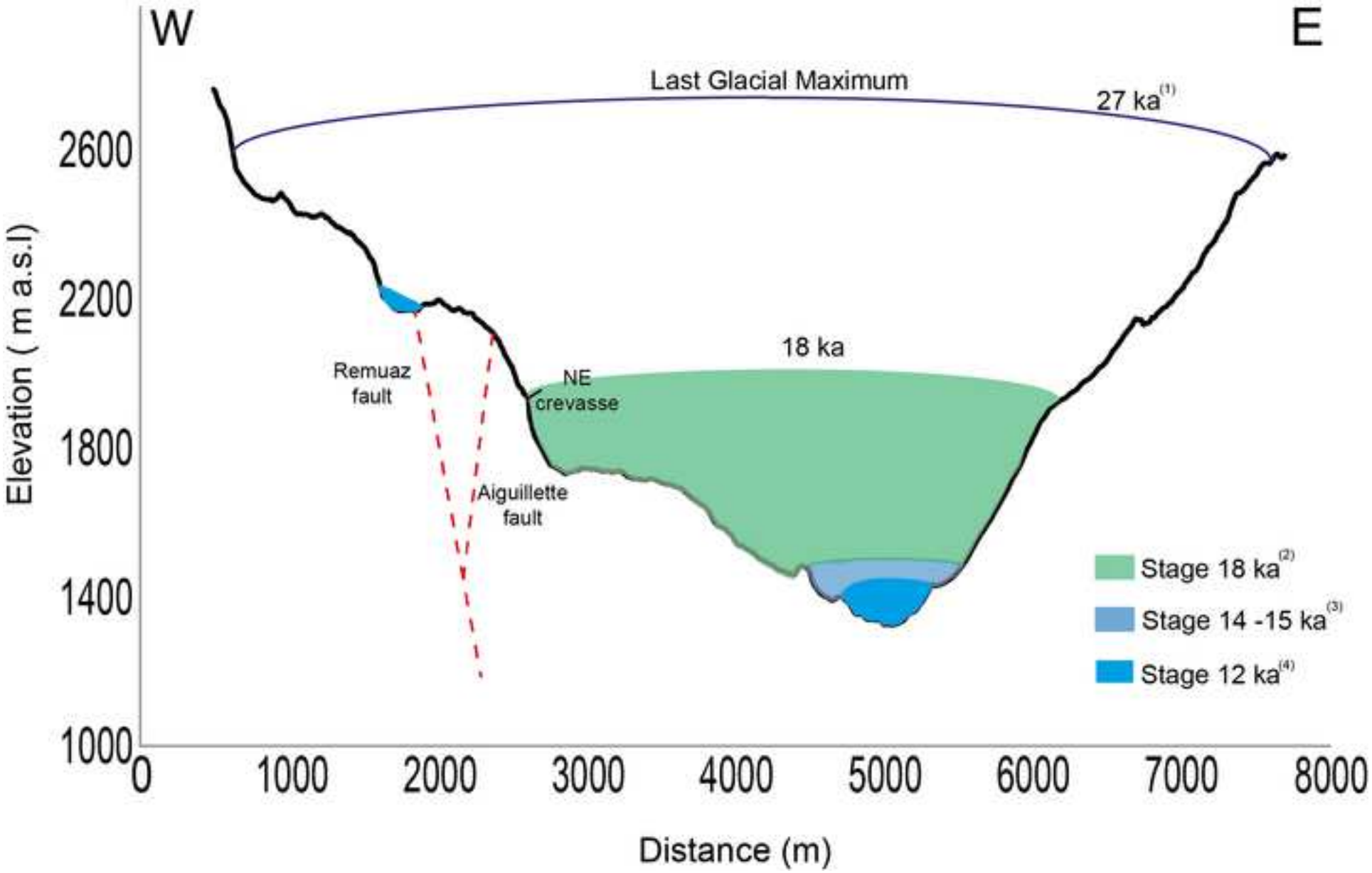

Figure9

Click here to access/download;Figure;Fig9_L_Courtial_Manent.png

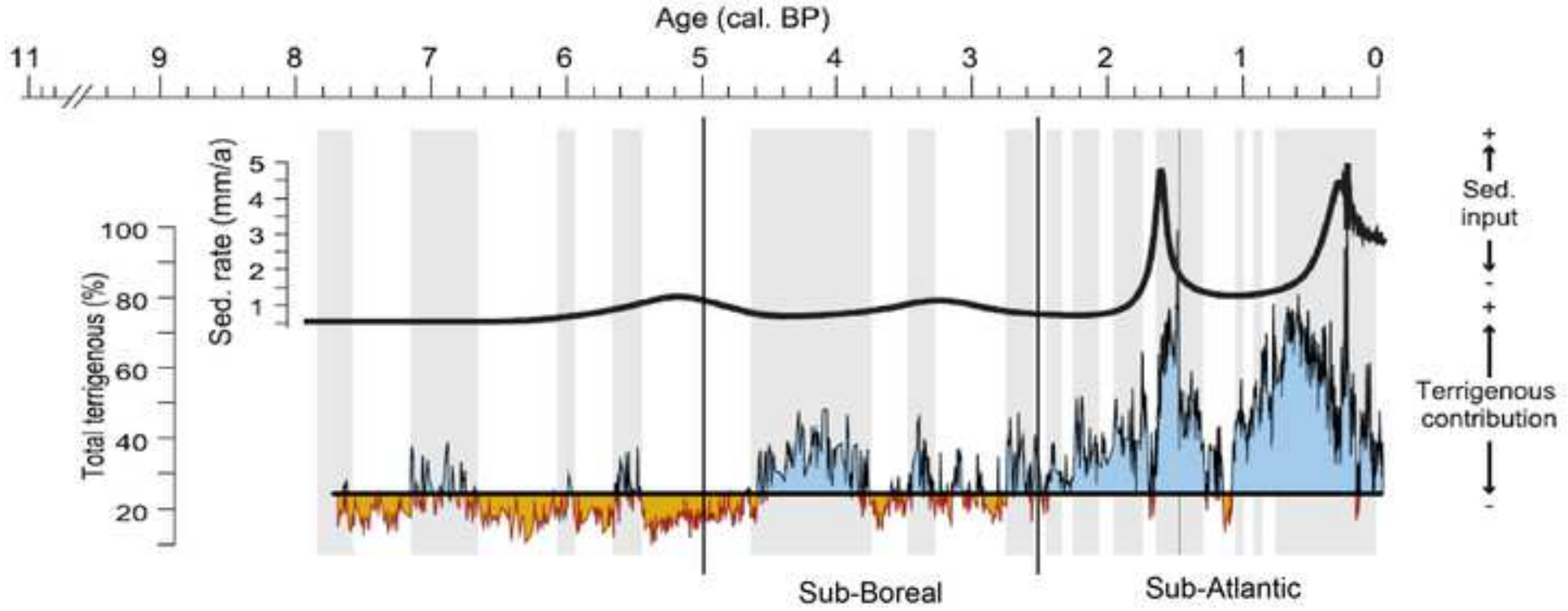

Table1

Site	Sample	Type	Latitude (dd)	Longitude (dd)	Elevation (m a.s.l)	*T* (cm)	Aspect (°)	*Z* (m)	Z_E (m)	S	M_{quartz} (g)	Carrier (mg ^{9}Be)	^{10}Be at x10^{5}	^{10}Be/^{9}Be x10^{-14}
NE crevasse (Profile P1)	AIG20-1	Scarp	45.982667	6.910054	1937	4	72	0.3	0.2	0.584	21.33	0.50	23.08	6.87 ± 0.26
	AIG20-2	Scarp			1936	4	72	1.8	1.5	0.584	16.90	0.50	3.07	0.92 ± 0.18
	AIG20-3	Scarp			1934	4	72	3.3	2.7	0.584	25.59	0.50	2.85	0.86 ± 0.17
	AIG20-4	Scarp			1933	4	72	4.3	3.5	0.584	22.17	0.51	2.09	0.61 ± 0.19
	AIG20-5	Scarp			1933	7	72	4.3	3.5	0.584	29.34	0.51	1.69	0.5 ± 0.23
	AIG20-6	Scarp			1931	6	72	6.6	5.3	0.584	29.22	0.50	1.13	0.34 ± 0.16
	AIG20-7	Polished bedrock	45.98186	6.910152	1895	4	60		0	0.682	35.86	0.50	44.57	13.4 ± 0.45
NE crevasse (Profile P2)	AIG20-16	Scarp	45.982404	6.910190	1933	3	70	2.1	1.8	0.584	28.07	0.52	2.44	0.71 ± 0.15
	AIG20-17	Scarp	45.982373	6.910219	1932	4	70	3.5	3	0.584	26.68	0.50	3.22	0.96 ± 0.15
	AIG20-18	Scarp	45.982353	6.910233	1930	4	70	5	4.3	0.584	38.37	0.50	3.30	0.99 ± 0.21
	AIG20-19	Scarp	45.982325	6.910252	1929	3	70	6.9	5.9	0.584	33.06	0.50	1.99	0.6 ± 0.18

Table

Site	*Displacement vector (norm)*	*Strike of displacement vector*	*Dip of displacement vector*	*Mean crevasse orientation*	*Mean dip of the crevasse (a)*	*Mean opening of the crevasse*
1	*12 m*	*N 100°*	*65°E*	*N164°E*	*72°E*	*1.5 m*
2	*13 m*	*N 130 °*	*50°E*	*N42°E*	*Vertical*	*10 m*
3	*7.2 m*	*N 102°*	*40°E*	*N8°E*	*65°E*	*3.7 m*
4	*3.7 m*	*N 115°*	*45°E*	*N22°E*	*67°E*	*2 m*

Table3

Sample	^{10}Be	^{10}Be age ± external uncertainty	Internal uncertainty	Inherited ^{10}Be concentration	Inheritance/ measured	Corrected concentration	Corrected age ± external uncertainty	Internal uncertainty (1σ)
	x10^4 at.g^{-1}	(ka)	(ka)	(at.g^{-1})	(%)	(at.g^{-1})	(ka)	(ka)
AIG20-1	19.30 ± 0.74	17.51 ± 1.01	0.65	-	-	-	-	-
AIG20-2	3.14 ± 0.60	3.01 ± 0.59	0.57	1,80E+04	57	1,35E+04	1.26 ± 0.30	0.29
AIG20-3	1.94 ± 0.39	1.84 ± 0.38	0.37	3,13E+03	16	1,62E+04	1.53 ± 0.33	0.31
AIG20-4	1.86 ± 0.58	1.76 ± 0.57	0.56	1,31E+03	7	1,73E+04	1.64 ± 0.52	0.52
AIG20-5	1.04 ± 0.48	1.01 ± 0.46	0.45	1,31E+03	13	9,07E+03	0.88 ± 0.40	0.40
AIG20-6	0.69 ± 0.32	0.66 ± 0.30	0.30	5,86E+02	6	6,32E+03	0.61 ± 0.27	0.29
AIG20-7	23.62 ± 0.81	18.87 ± 1.03	0.62	-	-	-	-	-
AIG20-16	1.65 ± 0.35	1.56 ± 0.34	0.34	1,13E+04	68	5,23E+03	0.48 ± 0.11	0.11
AIG20-17	2.37 ± 0.36	2.25 ± 0.36	0.35	2,44E+03	10	2,12E+04	2.01 ± 0.33	0.32
AIG20-18	1.65 ± 0.36	1.56 ± 0.35	0.34	8,17E+02	5	1,56E+04	1.47 ± 0.33	0.32
AIG20-19	1.00 ± 0.31	0.95 ± 0.29	0.29	5,37E+02	5	9,49E+03	0.89 ± 0.28	0.27